The Astronomical Journal, 154:39 (7pp), 2017 July https://doi.org/10.3847/1538-3881/aa738b

Near-IR Transmission Spectrum of HAT-P-32b using *HST*/WFC3

M. Damiano[1,2], G. Morello[1], A. Tsiaras[1], T. Zingales[1,2], and G. Tinetti[1]
[1] Department of Physics & Astronomy, University College London, Gower Street, WC1E 6BT London, UK; mario.damiano.15@ucl.ac.uk
[2] INAF—Osservatorio Astronomico di Palermo, Piazza del Parlamento 1, I-90134 Palermo, Italy
Received 2016 October 18; revised 2017 May 10; accepted 2017 May 14; published 2017 July 5

Abstract

We report here the analysis of the near-infrared transit spectrum of the hot Jupiter HAT-P-32b, which was recorded with the *Wide Field Camera 3* (WFC3) on board the *Hubble Space Telescope*. HAT-P-32b is one of the most inflated exoplanets discovered, making it an excellent candidate for transit spectroscopic measurements. To obtain the transit spectrum, we have adopted different analysis methods, both parametric and non-parametric (Independent Component Analysis, ICA), and compared the results. The final spectra are all consistent within 0.5σ. The uncertainties obtained with ICA are larger than those obtained with the parametric method by a factor of ∼1.6–1.8. This difference is the trade-off for higher objectivity due to the lack of any assumption about the instrument systematics compared to the parametric approach. The ICA error bars are therefore worst-case estimates. To interpret the spectrum of HAT-P-32b we used $\mathcal{T}$-REx, our fully Bayesian spectral retrieval code. As for other hot Jupiters, the results are consistent with the presence of water vapor ($\log H_2O = -3.45^{+1.83}_{-1.65}$), clouds (top pressure between 5.16 and 1.73 bar). Spectroscopic data over a broader wavelength range are needed to de-correlate the mixing ratio of water vapor from clouds and identify other possible molecular species in the atmosphere of HAT-P-32b.

Key words: methods: data analysis – planets and satellites: atmospheres – planets and satellites: individual (HAT-P-32 b) – techniques: spectroscopic

1. Introduction

In the past decade the *Hubble Space Telescope* (*HST*) has been an invaluable observatory from which to study the properties of exoplanetary atmospheres. The majority of the planets observed to date are hot and gaseous, as they are the easiest targets to probe. Transit observations in the UV, VIS, and IR have started to provide important insights into the chemical composition and structure of the atmospheres of gas giants orbiting very close to their star. Many of these atmospheres appear to be in the hydrodynamic escape regime given their vicinity to the stellar host (e.g., Vidal-Madjar et al. 2003; Linsky et al. 2010). Common atmospheric components detected include alkali metals (e.g., Charbonneau et al. 2002; Redfield et al. 2008) and water vapor (e.g., Barman 2007; Tinetti et al. 2007; Grillmair et al. 2008; Deming et al. 2013; Fraine et al. 2014; Kreidberg et al. 2014). Condensates or hazes have also been identified (e.g., Knutson et al. 2014; Sing et al. 2016). Some of the data also suggest that carbon-bearing or more exotic species, such as TiO and VO (e.g., Swain et al. 2009; Snellen et al. 2010; Evans et al. 2016; Line et al. 2016), are present in some of these atmospheres. Finally, eclipse and phase curve observations have enabled us to glimpse into the atmospheric thermal properties and global circulation of a few of these objects (e.g., Majeau et al. 2012; Stevenson et al. 2014).

In this work we analyze the near-infrared transit spectrum of the hot Jupiter HAT-P-32 b ($T_{eq} = 1786$ K; Hartman et al. 2011) obtained with the WFC3 camera on board the *HST*. HAT-P-32b is one of the most inflated exoplanets discovered, being less massive than Jupiter ($M_p = 0.79\ M_{Jup}$) but having almost twice its radius ($R_p = 1.789\ R_{Jup}$). The atmosphere of HAT-P-32b has been observed with ground-based instruments in the optical wavelengths, revealing a featureless transmission spectrum (Gibson et al. 2013; Zhao et al. 2014; Mallonn & Strassmeier 2016; Nortmann et al. 2016). In addition, Zhao et al. (2014) suggested the presence of a thermal inversion in the atmosphere of HAT-P-32b to interpret eclipse observations.

We used our dedicated WFC3 pipeline (Tsiaras et al. 2016b) to extract the transit light curves per wavelength channel and obtain the planetary spectrum (Section 2). We used in parallel Independent Component Analysis to correct for the instrumental systematics, and investigated the effect of different analysis techniques on the same data set (Section 3). The final spectrum was analyzed using our fully Bayesian spectral retrieval code, $\mathcal{T}$-REx (Waldmann et al. 2015a, 2015b).

2. Data Analysis

2.1. Observations

The spatially scanned spectroscopic images of HAT-P-32b were obtained with the G141 grism and are available from the MAST archive[3] (ID:14260, PI: Deming Drake). The data set contains five consecutive *HST* orbits and each exposure is the result of 14 non-destructive reads, with a size of 256 × 256 pixels in the SPARS10 mode (exposure time = 88.435623 s). With this configuration the maximum signal level is 2.6×10^4 electrons per pixel and the total scan length is approximately 40 pixels.

During the light curve analysis, the first of the five orbits was discarded. This is a standard practice for exoplanet transit observations (e.g., Deming et al. 2013; Huitson et al. 2013; Haynes et al. 2015; Tsiaras et al. 2016a), as the telescope needs to stabilize into its new position. Of the remaining four *HST* orbits, the first and the fourth provide the out-of-transit baseline, while the second and the third capture the transit. The data set contains, for calibration purposes, a non-dispersed (direct) image of the target, obtained using the F139N filter.

2.2. Extraction of Light Curves

Before extracting the light curves (white and spectral), all frames were reduced using the routines described in

[3] https://archive.stsci.edu/

Tsiaras et al. (2016b). HAT-P-32A has an M1.5 stellar companion, HAT-P-32B ($T_{\rm eff} = 3565 \pm 82$ K; Zhao et al. 2014). The dispersed signals from HAT-P-32A and HAT-P-32B are blended when using the scanning mode. However, these two stars are separated enough (2.″923 ± 0.″004, Zhao et al. 2014) to avoid blending when the differential reads (the difference between two consecutive non-destructive reads, or "stripes") are considered. For each stripe, we determined the photometric aperture, taking into account the wavelength-dependent photon trajectories (Tsiaras et al. 2016b) and obtained a set of 12 white light curves. The same criterion was used to extract the spectral light curves, obtaining a set of 12 time series for each one of the 20 spectral bins. The wavelength range of each bin was chosen in order to have a similar flux level across all bins.

2.3. Parametric Fitting

It is known that instrumental systematics (known as "ramps") affect the WFC3 infrared detector both in staring (Berta et al. 2012; Swain et al. 2013; Wilkins et al. 2014) and scanning modes (Deming et al. 2013; Knutson et al. 2014; Kreidberg et al. 2014; Tsiaras et al. 2016a, 2016b). The brighter the star, the stronger the ramps. In the case of HAT-P-32b, the host star is relatively faint ($K_{\rm mag} = 9.99$) so we did not expect very strong ramps.

We fitted the ramps on the white light curve using a similar approach to Kreidberg et al. (2014); i.e., we adopted an analytic function with two different types of ramps, short-term and long-term, to correct the data:

$$R(t) = (1 - r_a(t - t_v))(1 - r_{b1}e^{-r_{b2}(t-t_0)}) \quad (1)$$

where, t is the mid-time of each exposure, t_v is the time when the visit starts, t_0 is the time when each orbit starts, r_a is related to the long-term ramp, and r_{b1}, r_{b2} are related to the short-term ramp.

To model the transit light curve we used our Python package, PyLightcurve,[4] which returns the flux as a function of time using the nonlinear limb-darkening law (Claret 2000). The limb-darkening coefficients were fitted on the profile of a star similar to HAT-P-32A ($T_* = 6207$ K, [Fe/H] $= -0.04$ dex, $\log(g_*) = 4.33$ [cgs]), using a modified version of the ATLAS stellar model described in Howarth (2011). In this fit we took into account the variable sensitivity of the G141 grism across its wavelength range. The observations do not cover both the ingress and the egress of the transit, hence we could not fit for the semi-major axis and inclination, which have been fixed to the values reported in Table 1. We also assumed a circular orbit. The results are shown in Figure 1 and reported in Table 2. As can be seen in the residuals near the egress, there are a few points that appear to deviate significantly from the model fitted to the white light curve. The root mean square (rms) of the residuals is 180 ppm, significantly higher than the photon-noise limited rms of 100 ppm. The error bar in transit depth is accordingly higher than the photon-noise limited case. This behavior could be caused by star-spots, which notoriously might generate a wavelength-dependent astrophysical signal and therefore a distortion on the spectrum. However, we repeated the analysis excluding these points and the spectrum was not affected. We also tested changing the orbital parameters up to 1σ, in both directions, from their reference values. However, this did not improve the white light curve residuals. The main effect was a shift of ∼120 ppm in the white light curve transit depth—i.e., up to 1.3σ from our reported uncertainty—but again no detectable effect on the spectrum (differential transit depths vary by less than 0.25σ on average).

[4] https://github.com/ucl-exoplanets/pylightcurve

Table 1
Parameters of the HAT-P-32b System (Hartman et al. 2011)

Stellar Parameters	
[Fe/H] [dex]	-0.04 ± 0.08
$T_{\rm eff}$ [K]	6207 ± 88
M_* [$M_\odot$]	1.160 ± 0.041
R_* [$R_\odot$]	1.219 ± 0.016
$\log(g_*)$ [cgs]	4.33 ± 0.01
Planetary Parameters	
$T_{\rm eq}$ [K]	1786 ± 26
$M_{\rm p}$ [$M_{\rm Jup}$]	0.860 ± 0.164
$R_{\rm p}$ [$R_{\rm Jup}$]	1.789 ± 0.025
a [AU]	0.0343 ± 0.0004
Transit Parameters	
T_0 [BJD]	$2454420.44637 \pm 0.00009$
Period [days]	2.150008 ± 0.000001
$R_{\rm p}/R_*$	0.1508 ± 0.0004
a/R_*	$6.05^{+0.03}_{-0.04}$
i [deg]	88.9 ± 0.4

Finally, for each wavelength bin we divided the spectral light curve by the white light curve (Kreidberg et al. 2014) and fitted a linear trend simultaneously with a relative transit model:

$$n_\lambda(1 + \chi_\lambda)(F_\lambda/F_W) \quad (2)$$

where n_λ is the normalization factor that needs to be calculated for each bin, χ_λ is the wavelength-dependent linear ramp (Tsiaras et al. 2016b, 2016a), and (F_λ/F_W) is the ratio between the spectral light curve and the white light curve. We fitted this model using the same orbital parameters listed in Table 1 and the white R_P/R_* ratio obtained from the white light curve fitting. The limb-darkening coefficients were calculated for each bin using the same method as for the white light curve (see Table 4). The rms of the residuals for the spectral light curves (on average 474 ppm) is close to the photon-noise limited case (on average 443 ppm). The corresponding error bars in relative transit depths are also ∼10% above the photon noise limit. This proves that the deviation from the model seen for the white light curve is not wavelength dependent.

The planetary spectrum was fitted using MCMC and following two different approaches, leading to a "stacked" and a "weighted" spectrum:

1. (stacked) using a unique reference light curve for each spectral bin, obtained by summing the relative stripe light curves;
2. (weighted) fitting each stripe light curve alone, then taking the weighted mean for each spectral bin.

Following the first method, we obtained the white light curve shown in Figure 1 (top panel). Both methods give the same modulation, with the exception of a few bins where the differences are within 0.3σ.

3. ICA

Independent component analysis (ICA) is a blind signal-source separation (BSS) technique that is able to separate the

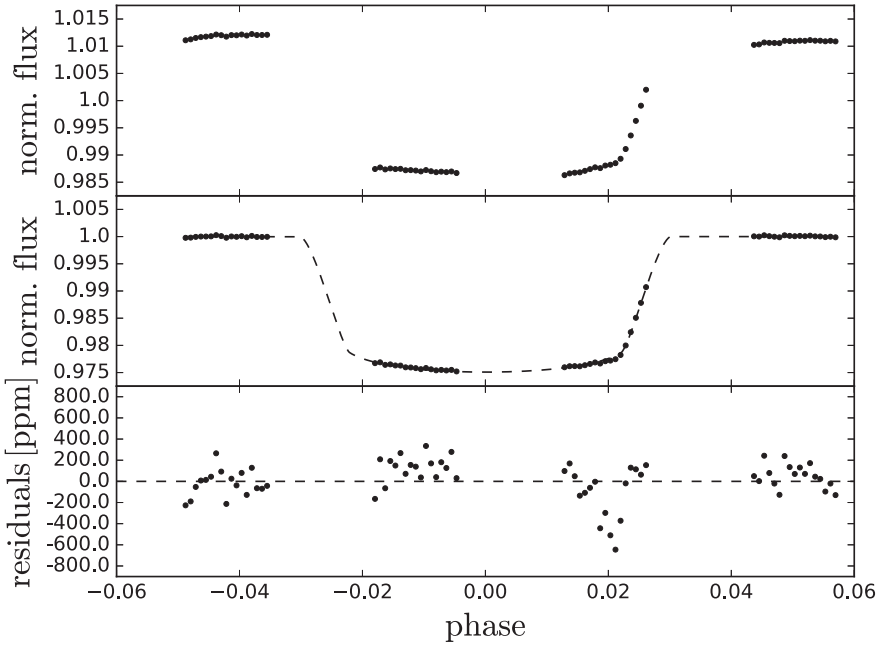

Figure 1. Top panel shows the white light curve of HAT-P-32b. The middle panel shows fitted white light curve. The bottom panel shows residuals after fitting.

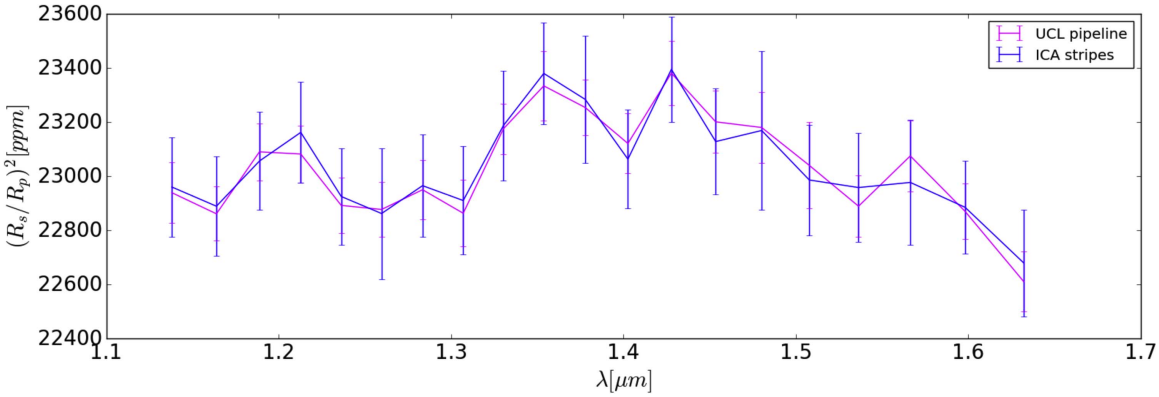

Figure 2. Stacked spectra obtained with the UCL pipeline (magenta) and with stripe-ICA (blue).

Table 2
White Light Curve Fitting Results

Limb-darkening Coefficients (1.125–1.650 μm)	
a_1	0.603336
a_2	−0.223032
a_3	0.281379
a_4	−0.13988
Fitting Results	
T_0 (HJD)	2457408.95783 ± 0.00004
R_p/R_*	0.1521 ± 0.0003

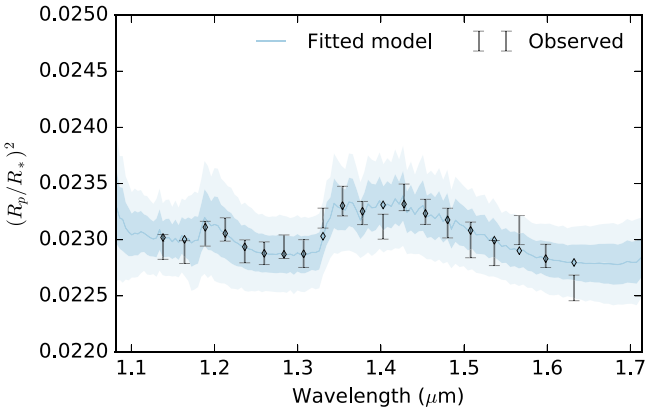

Figure 3. Transmission spectrum of HAT-P-32b obtained with the UCL pipeline (black) and best-fitting model (light-blue).

source signals in a set of observations without any prior knowledge about the signals themselves or their mixing ratios. In many applications, observations are well-represented as linear combinations of certain (unknown) source signals:

$$\boldsymbol{x} = \boldsymbol{A}\boldsymbol{s} \tag{3}$$

where $\boldsymbol{x} = (x_1, x_2,\ldots,x_n)^T$ is the column vector of observed signals, $\boldsymbol{s} = (s_1, s_2,\ldots,s_n)^T$ is the column vector of source signals, and $\boldsymbol{A}$ is the so-called mixing matrix. The original source signals are retrieved through a linear transformation that maximizes their

Table 3
Limb-darkening Coefficients a_{1-4} and Transit Depth $(R_p/R_*)^2$ for the Wavelength Channels

$\lambda_1 - \lambda_2$ (μm)		a_1	a_2	a_3	a_4	$(R_p/R_*)^2$ (ppm) UCL Pipeline	$(R_p/R_*)^2$ (ppm) Stripe-ICA
1.1250	1.1511	0.632741	−0.481904	0.701108	−0.306091	22940 ± 112	22961 ± 184
1.1511	1.1767	0.619205	−0.434713	0.64011	−0.282483	22862 ± 100	22890 ± 184
1.1767	1.2011	0.614294	−0.41589	0.610565	−0.272242	23091 ± 105	23057 ± 181
1.2011	1.2247	0.599151	−0.360648	0.544934	−0.247917	23083 ± 105	23163 ± 186
1.2247	1.2480	0.584001	−0.29953	0.465487	−0.216442	22893 ± 102	22926 ± 179
1.2480	1.2716	0.581928	−0.282551	0.441745	−0.210655	22878 ± 102	22863 ± 242
1.2716	1.2955	0.58946	−0.229732	0.322997	−0.169253	22951 ± 110	22966 ± 189
1.2955	1.3188	0.57237	−0.227002	0.362724	−0.181489	22864 ± 123	22911 ± 200
1.3188	1.3421	0.569522	−0.202303	0.325228	−0.166816	23176 ± 94	23188 ± 203
1.3421	1.3657	0.564634	−0.163366	0.265035	−0.14235	23335 ± 129	23381 ± 189
1.3657	1.3901	0.561817	−0.127278	0.200548	−0.113503	23255 ± 103	23285 ± 236
1.3901	1.4152	0.561832	−0.0979712	0.148201	−0.0914278	23122 ± 111	23064 ± 182
1.4152	1.4406	0.572262	−0.100901	0.133369	−0.0848254	23382 ± 119	23396 ± 195
1.4406	1.4667	0.58462	−0.111943	0.124656	−0.0799948	23202 ± 115	23129 ± 196
1.4667	1.4939	0.600205	−0.136878	0.140204	−0.0874595	23181 ± 130	23170 ± 294
1.4939	1.5219	0.609784	−0.134319	0.11158	−0.0721681	23041 ± 160	22987 ± 204
1.5219	1.5510	0.626375	−0.139701	0.0839621	−0.0555132	22890 ± 114	22959 ± 201
1.5510	1.5819	0.647904	−0.193435	0.120068	−0.0635888	23076 ± 131	22978 ± 230
1.5819	1.6145	0.663831	−0.223633	0.124246	−0.0583813	22871 ± 102	22886 ± 171
1.6145	1.6500	0.686226	−0.267069	0.137329	−0.0557593	22611 ± 111	22680 ± 198

mutual independence, according to one or more statistical estimators (Hyvärinen & Oja 2000; Hyvärinen 2012):

$$\boldsymbol{s} = \boldsymbol{W}\boldsymbol{x} \tag{4}$$

ICA has been used to remove instrument systematics and other astrophysical signals in exoplanetary light curves obtained with *Kepler*, *HST*/NICMOS (Waldmann 2012; Waldmann et al. 2013), *Spitzer*/IRS (Waldmann 2014), and *Spitzer*/IRAC (Morello et al. 2014, 2015, 2016; Morello 2015) with excellent results. We refer the reader to those publications and the relevant cited literature for more technical details about ICA and the different implementations. In this paper, we discuss a similar approach to the analysis of spectroscopic time series obtained with *HST*/WFC3 using the scanning-mode technique. The main steps of the algorithm are:

1. ICA decomposition;
2. fitting;
3. finalizing the parameter error bars.

3.1. ICA Decomposition

After the preliminary reduction, we obtained 12 stripe light curves for each of the 20 spectral bins, as described in Section 2.2. We performed ICA for all bins separately, by using the corresponding 12 stripe light curves as input time series (vector $\boldsymbol{x}$ in Equation (3)). Similarly, the light curves integrated over the 20 spectral bins for each stripe were used as input white light curves. Thus, we obtained one set of components for each spectral bin and an additional set for the whole spectral range. The transit signal is mainly contained in the first components of all sets, while the other components are predominantly instrument systematics and noise.

3.2. Fitting

Following a standard ICA algorithm (e.g., Morello 2015; Morello et al. 2016), we simultaneously fitted a transit model (with the same parameters as in Section 2.3) and a linear combination of the non-transit components to the relevant raw light curves. We computed the "stacked" and a "weighted" spectra, as described in Section 2.3.

The residuals obtained for the stacked white light curve have been included as an additional component in the spectral fits. This step is equivalent to dividing by the white light curve as is done in the parametric fitting (see Section 2.3), in order to remove possible undetrended systematics common to all wavelengths.

The fitting process is as follows. First, we run a Nelder-Mead optimization algorithm to find the parameter values minimizing the fitting residuals, then we use them as starting values for a Markov Chain Monte Carlo (MCMC) calculation with 300,000 iterations. The likelihood's variance, σ_0^2, is initialized to the variance of the residuals, then updated at any iteration. The best-fitting parameters are estimated as $\mu_{\rm par} \pm \sigma_{\rm par,0}$, where $\mu_{\rm par}$ and $\sigma_{\rm par,0}$ are the mean value and standard deviation of the relevant parameter chain, respectively.

3.3. Final Error Bars

To fully account for the potential bias associated with the detrending technique, the final error bars are re-scaled with respect to the MCMC error bars inferred from the residuals only, by adding a $\sigma_{\rm ICA}^2$ term to the likelihood's variance:

$$\sigma_{\rm par} = \sqrt{\frac{\sigma_{\rm ICA}^2 + \sigma_0^2}{\sigma_0^2}}\,\sigma_{\rm par,0}. \tag{5}$$

The $\sigma_{\rm ICA}^2$ term is calculated as:

$$\sigma_{\rm ICA}^2 = \sum_j o_j^2\,{\rm ISR}_j \tag{6}$$

where ISR is the so-called interference-to-signal-ratio matrix computed with ICA, and o_j are the coefficients of the non-transit components. Simply put, the $\sigma_{\rm ICA}$ term is the weighted sum of the errors attributed to the independent components extracted with ICA. We refer the reader to Morello et al. (2015, 2016) for additional details.

The error bars for the weighted spectrum are calculated as the simple arithmetic means of the error bars derived from fitting the independent components to the single stripes. These are worst-case estimates, as they do not scale when combining the results from the stripes. Scaling the error bars would not be theoretically correct, as the individual fits are not independent, given that they adopt the same components, which are estimated using the information contained in all of the stripes. The error bars obtained with ICA are larger than the ones obtained with the parametric approach by a factor ∼1.6 (weighted) and ∼1.8 (stacked). Note that scaling the error bars in the weighted approach would have led to final error bars smaller than photon-noise limited.

4. Atmospheric Retrieval

To interpret the spectrum of HAT-P-32b, we use $\mathcal{T}$-REx (Waldmann et al. 2015a, 2015b), a Bayesian spectral retrieval code that uses line lists provided by ExoMol (Yurchenko et al. 2011; Tennyson & Yurchenko 2012; Barton et al. 2013; Barber et al. 2014; Yurchenko & Tennyson 2014), HITRAN (Rothman & Gordon 2009; Gordon et al. 2013), and HITEMP (Rothman & Gordon 2010). We assumed an atmosphere dominated by molecular hydrogen and helium, with a mean molecular weight of 2.3 amu. We considered as candidate trace gases a broad range of molecules, including H_2O, C_2H_2, CH_4, CO_2, CO, HCN, NH_3, VO, and TiO. The RobERt (Robotic Exoplanet Recognition, Waldmann 2016) module restricts the list of detectable molecules, based on the observed spectral pattern, to H_2O, TiO, and VO. Given the relatively narrow spectral range probed, we assumed an isothermal profile and molecular abundances constant with pressure. In addition, we set uniform priors to the fitted parameters, which were: the mixing ratios of the molecules (10^{-12}–10^{-1}), the effective temperature of the planet (1400–2100 K), the radius of the planet (1.56–2.10 $R_{\rm Jup}$), and the cloud top pressure (10^{-3}–10^{6} Pa).

In addition to our best-fit model, we fitted for a fully cloudy atmosphere (straight line), and an atmosphere that contains only H_2O as an active gas (no TiO and VO). We calculated the Bayes factors relative to the cloudy model as follows:

$$B_m = \log \frac{E_m}{E_c} \tag{7}$$

where E_m is the Bayesian evidence of the test model and E_c is the one of the cloudy model.

We found $B_m = 12.2$ for the pure-water model and $B_m = 12.3$ for the model that includes water, TiO, and VO. These values correspond to a 5.3σ detection of water, while they are inconclusive about the presence of TiO and VO (Trotta 2008).

5. Results

Figure 2 reports the stacked spectra obtained with the parametric pipeline and with stripe-ICA. Table 3 reports the numerical results. The four spectra, i.e., stacked and weighted obtained with the two detrending algorithms, are all consistent within 0.5σ (maximum discrepancy for a wavelength bin). Also, the error bars for the corresponding stacked and weighted spectra are similar, within less than 10% in average.

5.1. Retrieval Results

The transmission spectrum of HAT-P-32b and the best fit to it, retrieved with $\mathcal{T}$-REx, is shown in Figure 3. The best-fitting values and the posterior distributions are shown in Table 4 and Figure 4. With the exception of water vapor, the fitted values for all of the other molecular mixing ratios are smaller than 10^{-7}. This result means that they are not detectable from this data set. The water vapor mixing ratio oscillates, instead, between $\log H_2O = -3.45^{+1.83}_{-1.65}$ depending on the clouds' top pressure, which could occur between 5.16 and 1.73 bar. A strong correlation between the water vapor mixing ratio, the clouds' top pressure, planetary radius at 10 bar, and temperature is noticeable in Figure 4, indicating there is a degeneracy of solutions.

6. Discussion

6.1. Comparison between Detrending Algorithms

As mentioned in the previous section, the error bars obtained with ICA are larger by a factor of ∼1.6–1.8 compared to the ones obtained with the parametric fitting. The larger error bars obtained with ICA are the trade-off for higher objectivity, due to the lack of any assumption about the instrument systematics compared to the parametric approach. The ICA error bars are worst-case estimates. It is worth noting that the discrepancies between the spectra obtained with the different methods are smaller than the parametric error bars, suggesting that, in this case, the ICA error bars might be overly conservative.

6.2. Comparison with Other Observations

Previous ground-based observations of the transit of HAT-P-32b in the optical wavelengths (Gibson et al. 2013; Zhao et al. 2014; Mallonn & Strassmeier 2016; Nortmann et al. 2016) did not find evidence of spectral modulations due to molecules. Our cloud top pressure is consistent with their measurements within 1σ, hence the water detection in the infrared is not controversial.

6.3. Strong Water Feature

Water vapor has been detected, to date, in the atmospheres of about 10 hot Jupiters (Iyer et al. 2016). Stevenson (2016) identified two classes of hot Jupiters, essentially mostly cloudy or with a strong water signature. The observed trend suggests that hotter ($T_{\rm eq} > 700$ K) and more inflated ($\log g > 2.8$) planets are more likely to have a strong water signature than cooler and smaller ones, but the current sample is not statistically significant. In agreement with this scenario, we find that HAT-P-32b ($T_{\rm eq} = 1786$ K; $\log g > 2.8$) has one of the strongest water features so far detected (∼500 ppm, 5.3σ).

7. Conclusion

We have reported here the analysis of the near-infrared transit spectrum of the hot Jupiter HAT-P-32b, which was recorded with the WFC3 on board the *HST*.

To obtain the transit spectrum, we adopted different analysis methods, which include parametric and non-parametric techniques (ICA), and compared the results. The final spectra are all consistent within 0.5σ. The uncertainties obtained with ICA are larger than the ones obtained with the parametric method by a factor of ∼1.6–1.8. The larger uncertainties obtained with ICA are the trade-off for higher objectivity, due to the lack of any assumption about the instrument systematics compared to the parametric approach. The ICA uncertainties are therefore the worst-case estimates.

To interpret the spectrum of HAT-P-32b, we used $\mathcal{T}$-REx, a fully Bayesian spectral retrieval code.

As for other hot Jupiters, the results are consistent with the presence of water vapor ($\log H_2O = -4.66^{+1.66}_{-1.93}$) and probably

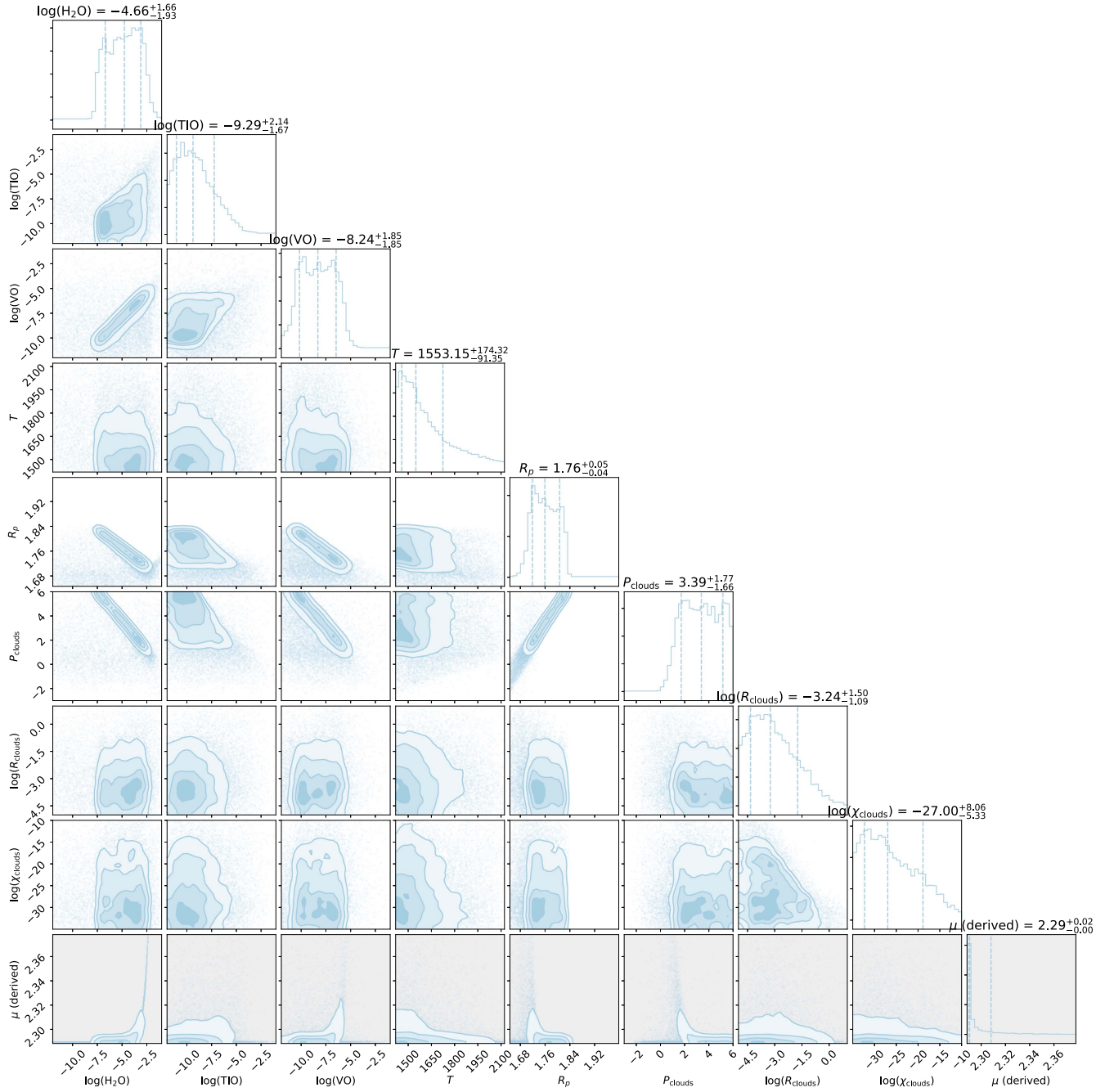

Figure 4. Posterior distributions to the fit for the WFC3 spectrum of the giant planet HAT-P-32b. Even though we tested the presence of many other molecules in this atmosphere, here we show only the posterior of H_2O because it is the only significant one. All of the other molecules do not show a statistically significant contribution to the fit.

Table 4
Fitting Results for HAT-P-32b Atmosphere

Parameter	Value
log H_2O	$-4.66^{+1.66}_{-1.93}$
$T_{\rm eff}$ [K]	1553^{+174}_{-91}
R_p [$R_{\rm jup}$]	$-1.76^{+0.05}_{-0.04}$
$P_{\rm cld,top}$ [bar]	$3.39^{+1.77}_{-1.66}$

clouds (top pressure between 5.16 and 1.73 bar). Spectroscopic data over a broader wavelength range will be needed to de-correlate the water vapor's mixing ratio from clouds and identify other possible molecular species in HAT-P-32b atmosphere.

The authors are supported by the European Research Council (ERC) grant 617119 *ExoLights*. M.D. and T.Z. are also supported by the Istituto Nazionale di AstroFisica—Osservatorio Astronomico di Palermo (INAF-OAPa). This work is also supported by STFC (ST/P000282/1).

The authors wish to thank Ingo Waldmann, Marco Rocchetto, Jonathan Tennyson, and Sergey Yurchenko for their input.

Appendix
Dilution Factor for the Companion Star

In this particular data set the nearby companion HAT-P-32B can be separated from the host star HAT-P-32A. This gives us

Table 5
Dilution Factor for the Nearby Companion in Each Wavelength Channel

$\lambda_1 - \lambda_2$ (μm)		Dilution Factor
1.1250	1.1511	0.03232 ± 0.00066
1.1511	1.1767	0.03272 ± 0.00068
1.1767	1.2011	0.03297 ± 0.00069
1.2011	1.2247	0.02607 ± 0.00043
1.2247	1.2480	0.02756 ± 0.00048
1.2480	1.2716	0.02845 ± 0.00051
1.2716	1.2955	0.02960 ± 0.00056
1.2955	1.3188	0.03050 ± 0.00059
1.3188	1.3421	0.03312 ± 0.00069
1.3421	1.3657	0.03318 ± 0.00070
1.3657	1.3901	0.03303 ± 0.00069
1.3901	1.4152	0.03307 ± 0.00069
1.4152	1.4406	0.03167 ± 0.00063
1.4406	1.4667	0.04220 ± 0.00113
1.4667	1.4939	0.04108 ± 0.00107
1.4939	1.5219	0.03937 ± 0.00098
1.5219	1.5510	0.03738 ± 0.00088
1.5510	1.5819	0.03602 ± 0.00082
1.5819	1.6145	0.03478 ± 0.00076
1.6145	1.6500	0.03412 ± 0.00074

the opportunity to calculate the dilution factor between the two stars, so that it can be used by other studies where the two stars cannot be separated. To calculate the dilution factor we extracted the light curve of the companion by adjusting the wavelength calibration and using an aperture expanding five pixels above and below the spatially scanned spectrum. Given the undispersed image of the system taken in the beginning of the observation, we found the companion to be shifted by −3.5487 and −23.9709 pixels along the horizontal and vertical axes of the detector, respectively. For this calculation we considered only the spectra obtained during the last *HST* orbit, as we noticed that the dilution factor was varying linearly during the two orbits before the transit. The most possible explanation for this behavior is the long-term linear ramp (see Table 5).

References

Barber, R. J., Strange, J. K., Hill, C., et al. 2014, MNRAS, 437, 1828
Barman, T. 2007, ApJL, 661, L191
Barton, E. J., Yurchenko, S. N., & Tennyson, J. 2013, MNRAS, 434, 1469
Berta, Z. K., Charbonneau, D., Désert, J.-M., et al. 2012, ApJ, 747, 35
Charbonneau, D., Brown, T. M., Noyes, R. W., & Gilliland, R. L. 2002, ApJ, 568, 377
Claret, A. 2000, A&A, 363, 1081
Deming, D., Wilkins, A., McCullough, P., et al. 2013, ApJ, 774, 95
Evans, T. M., Sing, D. K., Wakeford, H. R., et al. 2016, ApJL, 822, L4
Fraine, J., Deming, D., Benneke, B., et al. 2014, Natur, 513, 526
Gibson, N. P., Aigrain, S., Barstow, J. K., et al. 2013, MNRAS, 436, 2974
Gordon, I. E., Rothman, L. S., & Li, G. 2013, in International Symposium on Molecular Spectroscopy, 68th Meeting, abstract, #ERE03
Grillmair, C. J., Burrows, A., Charbonneau, D., et al. 2008, Natur, 456, 767
Hartman, J. D., Bakos, G. Á, Torres, G., et al. 2011, ApJ, 742, 59
Haynes, K., Mandell, A. M., Madhusudhan, N., Deming, D., & Knutson, H. 2015, ApJ, 806, 146
Howarth, I. D. 2011, MNRAS, 413, 1515
Huitson, C. M., Sing, D. K., Pont, F., et al. 2013, MNRAS, 434, 3252
Hyvärinen, A. 2012, RSPTA, 371, 20110534
Hyvärinen, A., & Oja, E. 2000, NN, 13, 411
Iyer, A. R., Swain, M. R., Zellem, R. T., et al. 2016, ApJ, 823, 109
Knutson, H. A., Benneke, B., Deming, D., & Homeier, D. 2014, Natur, 505, 66
Kreidberg, L., Bean, J. L., Désert, J.-M., et al. 2014, ApJL, 793, L27
Line, M. R., Stevenson, K. B., Bean, J., et al. 2016, AJ, 152, 203
Linsky, J. L., Yang, H., France, K., et al. 2010, ApJ, 717, 1291
Majeau, C., Agol, E., & Cowan, N. B. 2012, ApJL, 747, L20
Mallonn, M., & Strassmeier, K. G. 2016, A&A, 590, 100
Morello, G. 2015, ApJ, 808, 56
Morello, G., Waldmann, I. P., Tinetti, G., et al. 2014, ApJ, 786, 22
Morello, G., Waldmann, I. P., Tinetti, G., et al. 2015, ApJ, 802, 117
Morello, G., Waldmann, I. P., & Tinetti, G. 2016, ApJ, 820, 86
Nortmann, L., Palle, E., Murgas, F., et al. 2016, A&A, 594, 65
Redfield, S., Endl, M., Cochran, W. D., & Koesterke, L. 2008, ApJL, 673, L87
Rothman, L., & Gordon, I. 2010, in EGU General Assembly Conf. Abstracts (Vienna: EGU), 5561
Rothman, L. S., & Gordon, I. E. 2009, in International Symposium On Molecular Spectroscopy, 64th Meeting, abstract, #RI01
Sing, D. K., Fortney, J. J., Nikolov, N., et al. 2016, Natur, 529, 59
Snellen, I. A. G., de Kok, R. J., de Mooij, E. J. W., & Albrecht, S. 2010, Natur, 465, 1049
Stevenson, K. B. 2016, ApJL, 817, L16
Stevenson, K. B., Désert, J.-M., Line, M. R., et al. 2014, Sci, 346, 838
Swain, M., Deroo, P., Tinetti, G., et al. 2013, Icar, 225, 432
Swain, M. R., Vasisht, G., Tinetti, G., et al. 2009, ApJL, 690, L114
Tennyson, J., & Yurchenko, S. N. 2012, MNRAS, 425, 21
Tinetti, G., Vidal-Madjar, A., Liang, M.-C., et al. 2007, Natur, 448, 169
Trotta, R. 2008, ConPh, 49, 71
Tsiaras, A., Rocchetto, M., Waldmann, I. P., et al. 2016a, ApJ, 820, 99
Tsiaras, A., Waldmann, I. P., Rocchetto, M., et al. 2016b, ApJ, 832, 202
Vidal-Madjar, A., Lecavelier des Etangs, A., Désert, J.-M., et al. 2003, Natur, 422, 143
Waldmann, I. P. 2012, ApJ, 747, 12
Waldmann, I. P. 2014, ApJ, 780, 23
Waldmann, I. P. 2016, ApJ, 820, 107
Waldmann, I. P., Rocchetto, M., Tinetti, G., et al. 2015a, ApJ, 813, 13
Waldmann, I. P., Tinetti, G., Deroo, P., et al. 2013, ApJ, 766, 7
Waldmann, I. P., Tinetti, G., Rocchetto, M., et al. 2015b, ApJ, 802, 107
Wilkins, A. N., Deming, D., Madhusudhan, N., et al. 2014, ApJ, 783, 113
Yurchenko, S. N., Barber, R. J., & Tennyson, J. 2011, MNRAS, 413, 1828
Yurchenko, S. N., & Tennyson, J. 2014, MNRAS, 440, 1649
Zhao, M., O'Rourke, J. G., Wright, J. T., et al. 2014, ApJ, 796, 115